Validation of four-dimensional ultrasound for targeting in minimally-invasive beating-heart surgery

Danielle F. Pace[a,b], Andrew D. Wiles[a,c], John Moore[a], Chris Wedlake[a], David G. Gobbi[d] and Terry M. Peters[a,b,c]

[a]Imaging Research Laboratories, Robarts Research Institute, London, Ontario, Canada;
[b]Biomedical Engineering Graduate Program, [c]Department of Medical Biophysics,
The University of Western Ontario, London, Ontario, Canada;
[d]School of Computing, Queen's University, Kingston, Ontario, Canada

ABSTRACT

Ultrasound is garnering significant interest as an imaging modality for surgical guidance, due to its affordability, real-time temporal resolution and ease of integration into the operating room. Minimally-invasive intracardiac surgery performed on the beating-heart prevents direct vision of the surgical target, and procedures such as mitral valve replacement and atrial septal defect closure would benefit from intraoperative ultrasound imaging. We propose that placing 4D ultrasound within an augmented reality environment, along with a patient-specific cardiac model and virtual representations of tracked surgical tools, will create a visually intuitive platform with sufficient image information to safely and accurately repair tissue within the beating heart. However, the quality of the imaging parameters, spatial calibration, temporal calibration and ECG-gating must be well characterized before any 4D ultrasound system can be used clinically to guide the treatment of moving structures. In this paper, we describe a comprehensive accuracy assessment framework that can be used to evaluate the performance of 4D ultrasound systems while imaging moving targets. We image a dynamic phantom that is comprised of a simple robot and a tracked phantom to which point-source, distance and spherical objects of known construction can be attached. We also follow our protocol to evaluate 4D ultrasound images generated in real-time by reconstructing ECG-gated 2D ultrasound images acquired from a tracked multiplanar transesophageal probe. Likewise, our evaluation framework allows any type of 4D ultrasound to be quantitatively assessed.

Keywords: Validation/evaluation, ultrasound guidance, cardiac procedures, enhanced reality, intraoperative imaging, image-guided therapy, visualization

1. INTRODUCTION

Minimally-invasive cardiac surgery performed on the beating heart decreases patient trauma and the risk of side-effects compared with traditional cardiac surgery, where access to the heart is provided by a median sternotomy, the heart is arrested and blood circulation and oxygenation is accomplished using a cardiopulmonary bypass machine. Since direct vision of the surgical target, such as the mitral valve or an atrial septal defect, is impossible while delivering therapy within the closed chest, our group has developed a three-dimensional augmented reality environment integrating intraoperative transesophageal echocardiography (2D TEE), dynamic patient-specific heart models derived from preoperative images, and virtual representations of surgical tools that are tracked using a magnetic tracking device.[1]

Intraoperative 3D and 4D ultrasound imaging has shown great promise for interventional procedures, and for example has been used for therapy delivery to the brain,[2] liver[3] and prostate.[4] Ultrasound is low-cost and ubiquitous within operating rooms, and so our next step in improving our augmented reality environment is to provide volumetric intraoperative imaging using 4D ultrasound. Previous studies have shown that guidance using real-time 3D transthoracic echocardiography (3D TTE) alone is adequate for off-pump intracardiac surgery

Further author information: (Send correspondence to D.F.P.)
D.F.P.: E-mail: dpace@imaging.robarts.ca, Telephone: 1 519 663 5777 ext 34136
T.M.P.: E-mail: tpeters@imaging.robarts.ca, Telephone: 1 519 663 5777 ext 34159

employing a median sternotomy[5] and shows promise in minimally-invasive robotic cardiac surgery.[6] Instead of simply using the display on the ultrasound machine's monitor, we propose that placing 4D ultrasound within an augmented reality environment will mitigate several drawbacks associated with using echocardiography alone, including the lack of context surrounding the images and image interpretation challenges such as difficulties in distinguishing between surgical tools and the surrounding anatomy. Integrating 4D ultrasound into our system will amplify the intraoperative image information available for both visualization and for registration between the patient coordinate frame and those of preoperative images and derived models.

Since we are employing a minimally-invasive surgical access, we are constrained to the use of transesophageal probes and magnetic tracking, since transthoracic probes are cumbersome and maintaining a line of sight between a probe and an optical tracking system is difficult. In this paper, we focus on reconstructing a time series of 3D volumes representing the patient's heart over the cardiac cycle using tracked 2D transesophageal ultrasound and ECG-gating. Real-time 3D transesophageal echocardiography (3D TEE) is a burgeoning technology that has been recently introduced; however there will always be a place for reconstructed ultrasound to improve the field of view and to take advantage of 2D TEE's higher resolution compared to real-time 3D TEE. Additionally, in contrast to 2D TEE, real-time 3D TEE is not yet widely available within the operating suite. Regardless of the type of echocardiography employed, the system's ability to localize and delineate moving objects within the beating heart must be characterized before it is relied on for therapeutic use instead of for diagnosis alone.

In this paper, we present an accuracy assessment framework for 4D ultrasound systems that measures both trueness and precision when imaging moving targets. Standard accuracy assessment protocols for 2D and 3D ultrasound imaging, such as that introduced by Rousseau *et al.*[7] and further developed by Wiles *et al.*,[8] evaluate the quality of spatial and temporal calibration procedures by imaging stationary phantoms of known construction. Since the environment within the beating heart presents sources of error not present when imaging stationary anatomy, such as motion artifacts and inexact ECG-gating, we assess accuracy in a dynamic setting by using a robot to move a tracked phantom. In addition, we use the protocol to validate a new 3D and 4D ultrasound reconstruction system that we've developed which reconstructs in real-time and hence allows the operator to monitor and adjust the reconstruction acquisition while it is in progress.

2. METHODS

2.1 3D and 4D Ultrasound Reconstruction

To provide intraoperative imaging of the beating heart during minimally-invasive cardiac procedures, we have developed a software system that can reconstruct 3D and 4D ultrasound in real-time using a tracked 2D multiplanar ultrasound probe. 3D and 4D ultrasound reconstruction can be performed using freehand scanning, or, if using a multiplanar probe, by imaging around its rotational axis while keeping the probe relatively stationary. This paper focuses on the rotational acquisition approach, since a transesophageal probe's position within the patient's esophagus makes it difficult to manipulate the probe in the slow, controlled manner required to generate high-quality reconstructions with freehand scanning. To maximize image quality, we image using the smallest possible inter-slice distance, which is one degree for our probe.

A significant advantage of our system is that both 3D and 4D ultrasound are generated in real-time, allowing the operator to view the volume(s) as they are being reconstructed and to adjust the acquisition protocol accordingly. This was accomplished by extending the real-time 3D ultrasound reconstruction software first presented by Gobbi and Peters[9] (and later released to the community[10]) to support 4D ultrasound reconstruction. We also incorporated rotation of the imaging plane for use with multiplanar probes. Briefly, the original 3D reconstruction software accomplishes real-time reconstruction by splitting the four main tasks into separate synchronized threads: (1) buffering ultrasound video frames and their corresponding timestamps; (2) receiving and timestamping transforms from the tracking system; (3) updating pixels within the output in real-time and (4) visualizing the current state of the 3D volume. The acquisition time for static 3D ultrasound depends only on the time required for the operator to rotate 2D probe's imaging plane at one degree increments through 180 degrees, and is generally between 60-90 seconds.

In much the same way, 4D ultrasound reconstruction generates a time series of 3D volumes. An additional thread executes every 5 ms to monitor the patient's ECG signal for prospective ECG triggering. At each instance

of the automatically-detected trigger signal that indicates the beginning of a new cardiac cycle, the period of the previous cycle is used to predict the timestamps for the upcoming cycle that correspond to one of the N output volumes for phases 0 .. $N-1$. For each cardiac cycle, the ultrasound frames whose timestamps are closest to these predicted values are inserted into the correct output volume using the associated tracking transforms. A disadvantage of prospective ECG triggering is that changes in the patient's heart rate can cause ultrasound images corresponding to slightly different points in the cardiac cycle to be inserted into the same 3D volume, causing artifacts. To mitigate this effect, an expected heart rate is calculated prior to the 4D reconstruction procedure by averaging the heart rates recorded over a user-specified time period and with a user-specified allowed percentage deviation from the mean. A buffering scheme is used so that 2D images are inserted one cycle after they are acquired, allowing heart rates to be checked against the expected value and 2D images corresponding to unacceptably long or short cycles to be discarded before they are inserted. During the reconstruction, the 2D probe's imaging plane can be rotated at a maximum speed of once per cardiac cycle, so the minimum acquisition time is 180 multiplied by the cycle period. For example, a heart rate of 60 cycles/min leads to an acquisition time of at least three minutes.

2.2 The Dynamic Phantom

In order to assess the accuracy with which 3D and 4D ultrasound can be reconstructed, we have built a dynamic phantom (Figure 1a) comprised of a simple robot which moves a base to which one of three modular phantoms can be attached (Figure 1b): a *point-source phantom*, composed of a 2.45 mm diameter hard plastic polycarbonate sphere mounted upon a stainless steel pin above a small piece of sound absorbing material (Sorbothane Inc., Ohio, USA), a *distance phantom*, composed of four similar polycarbonate spheres arranged in a ramp configuration above two pieces of sound absorbing material (inspired by the wedge phantom presented by Barratt *et al.*[11]), and a hollow *spherical phantom* consisting of a 40.25 mm diameter table tennis ball fixed upon a nylon screw. To emulate the moving anatomy within the beating heart, we programmed a custom-built robot (LEGO® Mindstorms NXT™, The LEGO Group, Denmark) to move the phantom around a circular path of diameter 2.4 cm at a constant speed using an open-source robot control library.[12] As part of the accuracy assessment protocol described below, a 6-DOF sensor is connected to the phantom so that its position can be tracked using a magnetic tracking system.

Within the operating room, the current phase of the patient's heart within the cardiac cycle is determined by analysis of the ECG signal. To mimic this in the dynamic phantom, the light sensor of the LEGO® Mindstorms NXT™kit was positioned so that the emitted LED light is reflected off of one of the moving white beams on the phantom's base. This results in a signal from the sensor's phototransistor that varies predictably as the phantom moves. The beginning of a new cycle is automatically detected when the difference between the minimum and maximum light signal within a predefined time interval exceeds an empirically-determined threshold that depends on motor speed (Figure 1c).

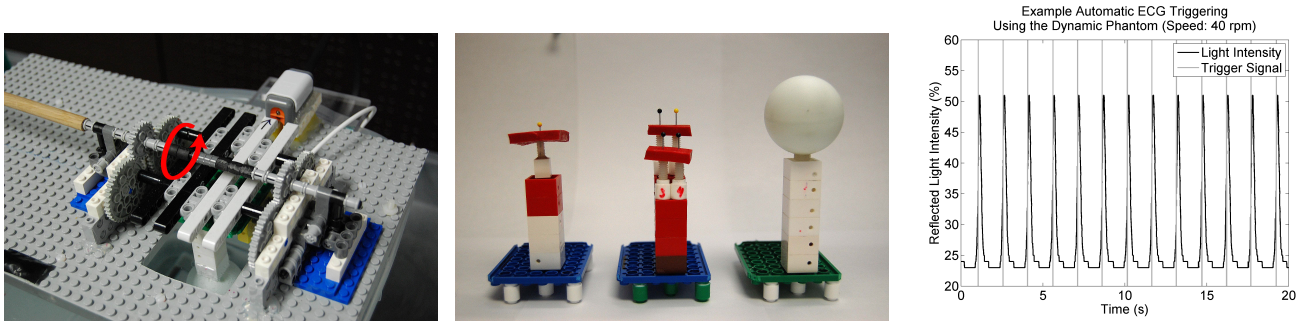

Figure 1: (left) The dynamic phantom, annotated to show the direction of phantom movement; (center) The point-source, distance and spherical phantoms; (right) Example light sensor signal, with automatically-detected ECG trigger signals that indicate the beginning of a new cycle.

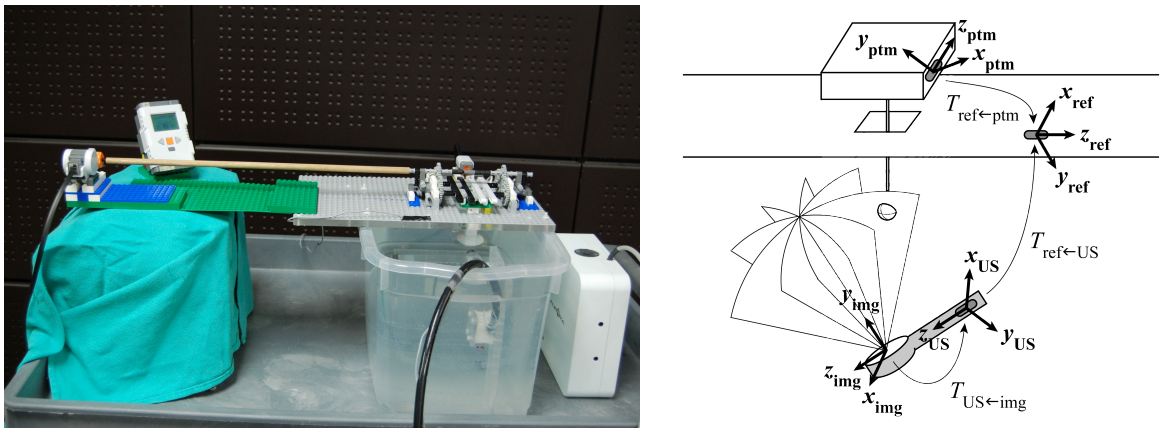

Figure 2: (left) The experimental setup; (right) Schematic illustrating the transformations used to calculate the expected position of the phantom within the image coordinate system. In the diagram, the phantom intersects the 90° plane of the multiplanar transducer, which lies along the **yz**-plane of the image coordinate system).

2.3 The Accuracy Assessment Protocol

The experimental setup, shown in Figure 2a, consisted of a 3.2 GHz dual-CPU machine with 2 GB RAM running the reconstruction software, a Philips Sonos 7500 ultrasound machine from which a frame grabber records 640x480 frames with 0.3464 mm pixels at 30 Hz, a Philips adult transesophageal echo transducer (M/N:T6210) that could be secured at varying height and orientation, the dynamic phantom and the Aurora magnetic tracking system (Northern Digital Inc., Waterloo, Canada). Two 6-DOF sensors, one fixed to the ultrasound probe and another attached to the phantom, are tracked relative to a 6-DOF reference sensor (Northern Digital Inc., Waterloo, Canada; Traxtal, Toronto, Canada). Prior to imaging, a spatial calibration must be performed to determine the transformation from the sensor mounted on the ultrasound probe to the ultrasound probe's fan origin, and the temporal lag between video frames and their corresponding tracking transformations must be found using temporal calibration. Both of these calibrations were performed using previously-published techniques: spatial calibration using a Z-bar phantom[13] and temporal calibration using a cross-string technique.[14]

We performed multiple 3D and 4D acquisitions for each phantom using the calibration matrix resulting from a single spatial calibration and the same temporal lag time. Twenty-five static 3D ultrasound volumes were reconstructed for each phantom at varying depths (i.e. distance from the transducer) and probe orientations, with an isotropic voxel size of 0.3464 mm (resampled to an isotropic voxel size of 0.6928 mm before subsequent analysis). For each phantom, a dynamic 4D acquisition comprising five 3D volumes was performed for two depths at each of five speeds (20, 30, 40, 50 and 60 rpm, corresponding to 2.5, 3.8, 5.0, 6.3 and 7.5 cm/s, respectively). The 4D reconstructions were created by rotating the transducer's imaging plane by one degree approximately once every two cycles. These volumes were reconstructed directly with an isotropic voxel size of 0.6928 mm with a 1.5% allowed deviation from the expected cycle frequency. To approximate the speed of sound in tissue, all experiments were performed within a bath of 7% glycerol solution.

To determine the reconstruction accuracy, we calculated the expected phantom position for each image based on the phantom's structure and the position of the attached sensor, and compared it to a manual segmentation of the images. The process of deriving the expected phantom position within the image coordinate system proceeded as follows and is depicted in Figure 2b:

- *Micro-CT*: We acquired a micro-CT image of each phantom and manually created a set of 3D coordinates that outlined the phantom's sphere(s). The center $\mathbf{p}_{mCT}$ and radius $\mathbf{r}_{mCT}$ of each sphere was then found using a least-squares sphere-fit algorithm.[15]
- *Point-based registration*: Each phantom is equipped with ten divots, which were manually identified in the micro-CT image and localized relative to the sensor mounted on the phantom using a tracked pointer tool. The transformation $\mathbf{T}_{ptm \leftarrow mCT}$ was subsequently found using a point-based linear registration.

- *Magnetic tracking*: The transformations $\mathbf{T}_{ref \leftarrow ptm}$ and $\mathbf{T}_{ref \leftarrow US}$ result from tracking the sensors mounted on the phantom and ultrasound probe relative to the reference sensor. When these transformations are approximately constant throughout the acquisition (i.e. $\mathbf{T}_{ref \leftarrow US}$ during 3D and 4D reconstructions and $\mathbf{T}_{ref \leftarrow ptm}$ during 3D reconstructions) we use the transformation that gives rise to the median coordinate. Assuming that the motor operates at a constant speed, $\mathbf{T}_{ref \leftarrow ptm}$ is calculated for each phase of a 4D ultrasound reconstruction assuming that the motor operates at a constant speed by (1) finding the median transformation of those identified by the reconstruction software as corresponding to phase 0; (2) projecting all tracking coordinates onto the 2D plane defined by the two principal eigenvectors found by applying a principal component analysis to all of the tracking data; (3) subdividing the best-fit circle of the 2D data into evenly spaced sections starting at the projection of the phase 0 point found in step (1); and (4) projecting the points back into the original 3D space. The RMS Euclidean distance between these coordinates and the median coordinates for each phase are approximately 0.75 mm for all three phantoms, with a maximum of 1.2 mm over all trials.

- *Calculating the expected position*: Finally, the spatial calibration matrix gives the transformation $\mathbf{T}_{US \leftarrow img}$ from the fan origin within the 2D images to the sensor mounted on the ultrasound probe, so the expected position of the phantom $\mathbf{p}_{exp}$ within the image coordinate system is given by

$$\mathbf{p}_{exp} = {\mathbf{T}^{-1}}_{US \leftarrow img} \bullet {\mathbf{T}^{-1}}_{ref \leftarrow US} \bullet \mathbf{T}_{ref \leftarrow ptm} \bullet \mathbf{T}_{ptm \leftarrow mCT} \bullet \mathbf{p}_{mCT} \quad (1)$$

  The axes of the image coordinate system are defined by the ultrasound beam at 0° rotation, such that the **x**-axis points in the lateral direction, the **y**-axis points in the axial (depth) direction, and the **z**-axis points in the elevation direction (see Figure 2b). During the image acquisitions, the ultrasound transducer is positioned so that the plane of the phantom's circular movement lies approximately parallel to the **yz** plane.

The acquired image volumes were characterized by a single user, who marked both the center of the bright spots representing the spheres on the point-source and distance phantoms and points on the spherical phantom's

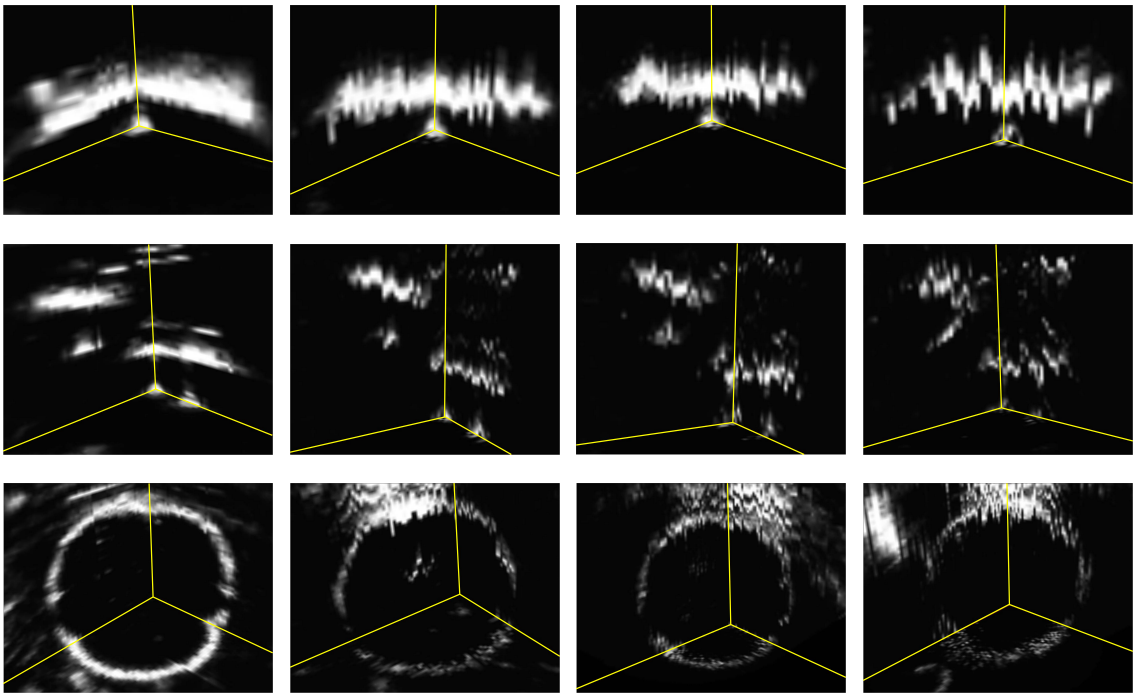

Figure 3: Example reconstructions of the point-source (top), distance (middle) and spherical (bottom) phantoms. Column one shows 3D reconstructions of a static phantom, while columns 2-4 show the phase 0 volumes from ultrasound reconstructions of a dynamic phantom moving at 20, 40 and 60 rpm, respectively.

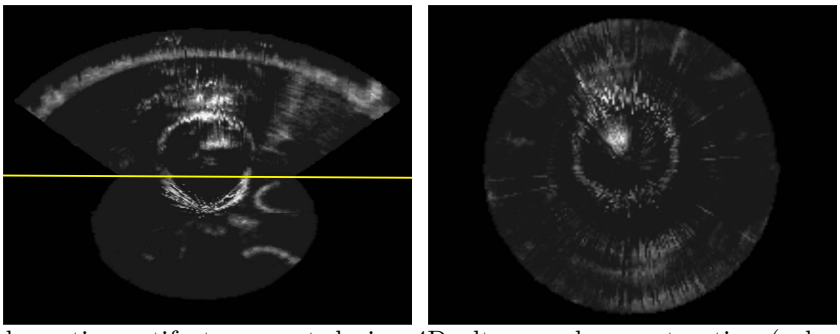

Figure 4: Example motion artifacts present during 4D ultrasound reconstruction (spherical phantom at 50 rpm).

outline on the edges closest to the transducer's fan origin. The user dealt with the motion artifacts present in the 4D ultrasound volumes by attempting to choose the center of of the cloud of bright pixels for the point-source and distance phantoms, and by tracing a smooth curve for the spherical phantom. The single coordinates representing each sphere on the point-source and distance phantoms were taken directly as the observed phantom coordinates $\mathbf{p}_{obs}$ for comparison to the expected phantom positions, while the points outlining the spherical phantom were input to an ellipsoid-specific fitting algorithm.[16] Note that this algorithm's assumption that the length of the ellipsoid's minor axis is at least half that of its major axis will be true for all images of our spherical object. Finally, we followed the method described by Schneider and Eberly[17] to extract the center, three radii lengths and three eigenvalues corresponding to the best-fit ellipsoid.

3. RESULTS

Example 3D and 4D reconstructions of the three phantoms are shown in Figure 3: qualitatively, the image volumes generated by our real-time reconstruction system show good correspondence to the actual phantom structures. As is typical for such ECG-gated systems, the 4D ultrasound reconstructions suffer from motion artifacts that radiate from the rotational axis and become more prominent with increasing phantom speed. Figure 4 depicts further examples of these artifacts, which are further discussed in Section 4.

3.1 Accuracy measurements

All imaging systems that are intended for interventional guidance are subject to the constraints on procedural accuracy that must be satisfied for positive clinical outcomes, and hence their performance must be fully studied before they are used therapeutically. To quantify the error sources present in our 3D and 4D ultrasound reconstruction system, we compared the expected and observed phantom characterizations with respect to localization, distance, volume and shape. Sample comparisons are depicted in three dimensions in Figure 5.

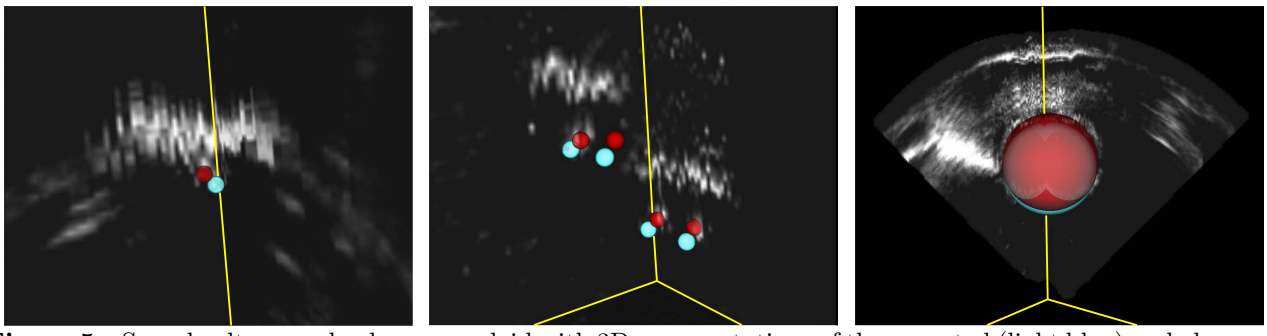

Figure 5: Sample ultrasound volumes overlaid with 3D representations of the expected (light blue) and observed (red) phantom positions for the point-source (left), distance (center) and spherical (right) phantoms.

Table 1: Summary statistics for center reconstruction error over N trials.

	Center Reconstruction Error (mm)							
	Static Phantom (3D US)				Dynamic Phantom (4D US)			
Direction	RMS	Mean	Std Dev	N	RMS	Mean	Std. Dev.	N
	Point-Source Phantom							
Euclidean	1.54	1.46	0.50	25	2.68	2.54	0.87	50
X	0.67	0.25	0.64	25	0.77	-0.33	0.70	50
Y	1.17	0.99	0.64	25	1.73	1.18	1.28	50
Z	0.74	0.02	0.75	25	1.90	-0.68	1.79	50
	Distance Phantom							
Euclidean	1.72	1.59	0.65	100	2.53	2.39	0.81	200
X	0.93	0.38	0.86	100	0.51	-0.10	0.50	200
Y	0.99	0.82	0.57	100	1.62	0.91	1.34	200
Z	1.04	0.61	0.85	100	1.87	0.07	1.88	200
	Spherical Phantom							
Euclidean	1.22	1.18	0.30	25	2.71	2.54	0.95	50
X	0.69	-0.37	0.59	25	1.24	-1.12	0.54	50
Y	0.71	0.64	0.30	25	1.62	1.23	1.07	50
Z	0.71	-0.36	0.63	25	1.78	-0.57	1.70	50

For each phantom, we assessed the localization accuracy of our 3D and 4D ultrasound reconstruction system by comparing the expected and observed phantom centers. Table 1 lists summary statistics computed for the Euclidean center reconstruction error $CRE = \|\mathbf{p}_{obs} - \mathbf{p}_{exp}\|$ and for the errors along each of the three axes in the image coordinate system. For the 3D ultrasound reconstructions, the RMS Euclidean center reconstruction error ranged between 1.2 - 1.7 mm, with the spherical phantom giving both the least mean error and the least variability. The RMS Euclidean center reconstruction error for 4D ultrasound was similar for all three phantoms and ranged between 2.5 - 2.7 mm. Compared to the 3D reconstructions, both the magnitude and the variability of the error increased; for all three phantoms this was attributed first to increases in the mean and variability of the error in the **z**-direction, followed by increases in the **y**-direction. For both 3D and 4D ultrasound imaging and for all three phantoms, we also observed a bias towards overestimating the distance in the depth (**y**-) direction between the observed phantom center and the ultrasound fan origin.

To evaluate the accuracy with which distances are preserved, we calculated the distance reconstruction error $DRE = \|\mathbf{p_1}_{obs} - \mathbf{p_2}_{obs}\| - \|\mathbf{p_1}_{exp} - \mathbf{p_2}_{exp}\|$ for the two pairs of diagonally-opposite spheres on the distance phantom (Table 2). Although the expected Euclidean distance between each pair of spheres is the same for all image volumes, the expected distances in the **x**, **y** and **z** directions depend on the pose of the ultrasound transducer relative to the phantom. Since a single expected distance for each axis does not exist, we report these distance

Table 2: Summary statistics for distance reconstruction error over N trials (mean expected Euclidean distance = 21.0 mm). The use of percentages and the reasons for varying N are explained in Section 3.1.

	Distance Reconstruction Error (mm)							
	Static Phantom (3D US)				Dynamic Phantom (4D US)			
Direction	RMS	Mean	Std Dev	N	RMS	Mean	Std. Dev.	N
Euclidean	0.54	0.32	0.44	50	0.97	0.36	0.91	100
Euclidean (%)	2.70%	1.62%	2.19%	50	4.83%	1.80%	4.50%	100
X (%)	5.84%	3.65%	4.67%	21	7.51%	5.28%	5.40%	50
Y (%)	4.49%	3.04%	3.35%	42	7.12%	2.54%	6.69%	100
Z (%)	4.42%	-1.72%	4.17%	23	8.94%	-0.39%	8.98%	100

Table 3: Summary statistics for volume reconstruction error and eccentricity over N trials (expected volume = 34167.95 mm^3, expected radius = 19.59 mm).

	Radii Length Error (mm) and Volume Reconstruction Error (mm^3)							
	Static Phantom (3D US)				Dynamic Phantom (4D US)			
Measurement	RMS	Mean	Std Dev	N	RMS	Mean	Std. Dev.	N
Volume	5740.70	5675.43	881.03	25	5270.58	5145.77	1151.74	50
Volume (%)	18.24%	18.04%	2.80%	25	16.75%	16.35%	3.66%	50
Major	1.47	1.46	0.20	25	1.57	1.54	0.28	50
Medium	1.11	1.10	0.21	25	1.06	1.02	0.27	50
Minor	0.80	0.79	0.16	25	0.60	0.49	0.35	50

	Eccentricity (unitless)							
	Static Phantom (3D US)				Dynamic Phantom (4D US)			
Measurement	RMS	Mean	Std Dev	N	RMS	Mean	Std. Dev.	N
Medium Axis Ratio	0.98	0.98	0.009	25	0.98	0.98	0.016	50
Minor Axis Ratio	0.97	0.97	0.007	25	0.95	0.95	0.018	50
Fractional Anisotropy	0.034	0.033	0.007	25	0.057	0.053	0.021	50
Spherical Anisotropy	0.064	0.063	0.014	25	0.102	0.096	0.035	50

reconstruction errors as percent differences $\%_{DRE} = 100(\|\mathbf{p_{1}}_{obs} - \mathbf{p_{2}}_{obs}\| - \|\mathbf{p_{1}}_{exp} - \mathbf{p_{2}}_{exp}\|)/(\|\mathbf{p_{1}}_{exp} - \mathbf{p_{2}}_{exp}\|)$. Furthermore, $\%_{DRE}$ along an axis was calculated only when the expected distance along the axis was ≥ 10 mm, since small variations in the manual point-identification process manifest as substantial distance errors when the expected distance is very small. For both 3D and 4D ultrasound reconstruction, the distance reconstruction errors were much smaller than the center reconstruction errors, indicating that the relationships between objects are well-preserved despite any errors in their localization. The RMS Euclidean distance reconstruction error for 3D ultrasound reconstruction was 0.54 mm and increased to 0.97 mm for 4D ultrasound reconstruction. This

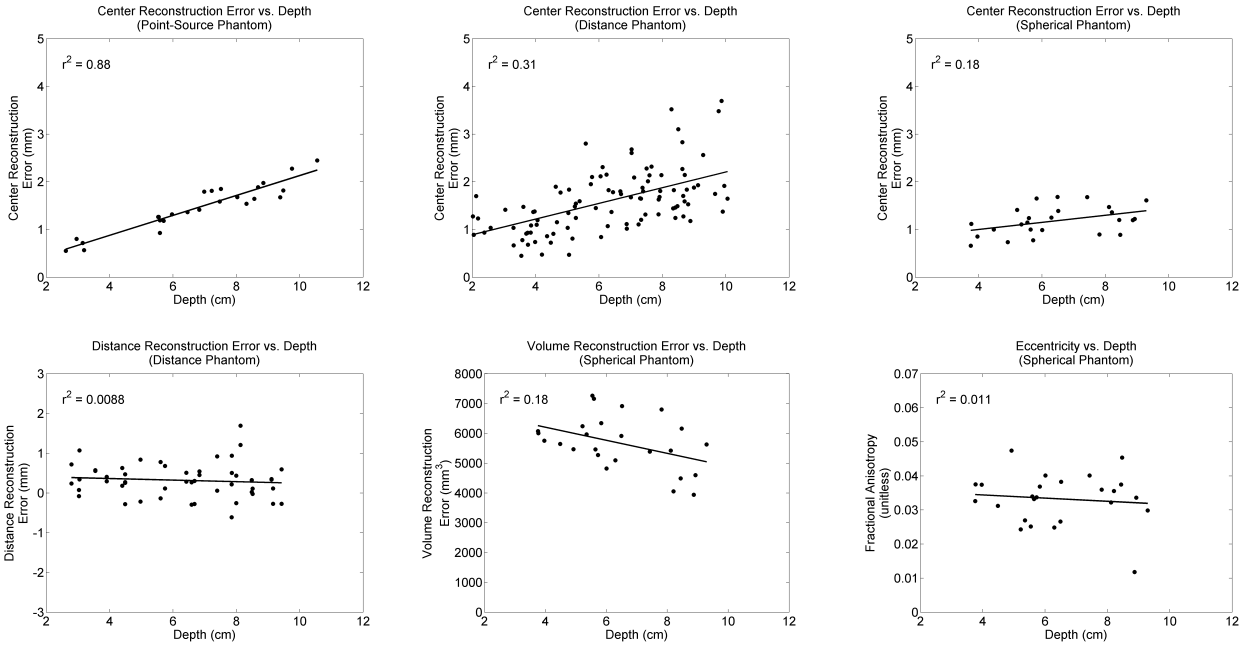

Figure 6: Center reconstruction error, distance reconstruction error, volume reconstruction error and fractional anisotropy for 3D ultrasound reconstruction versus distance from the transducer.

increase was attributed mostly to an increase in variability, which was most prominent in the **z**-direction. In both 3D and 4D ultrasound, there was a bias towards overestimating the Euclidean distance between objects, and we found no striking difference between the distance reconstruction errors in the **x**-, **y**- and **z** directions.

Using the spherical phantom, we determined the volume reconstruction error $VRE = v_{obs} - v_{exp}$ and the major, medium and minor radii length errors $(r_{maj} - r_{mCT})$, $(r_{med} - r_{mCT})$ and $(r_{min} - r_{mCT})$, by comparing the known structure of the table tennis ball to the parameters of the best-fit ellipsoids derived from the image data (Table 3). Volume was overestimated in every image volume analyzed, with RMS volume reconstruction errors for 3D and 4D ultrasound corresponding to percent differences of 18.24% and 16.75%, respectively. The magnitude of these errors indicate that our reconstructed image volumes should not be used for intracardiac volume measurements without caution, and, since the radii length errors are reasonable, arise from the cubed relationship between volume and radius length. The large volume reconstruction errors may also be partially due to the procedure used to manually outline the image of the spherical phantom, since the radii length errors were much larger than the Euclidean distance reconstruction errors despite the fact that the expected radius of the sphere is similar to the distances between the point pairs of interest in the dynamic phantom.

Finally, we evaluated object shape in our 3D and 4D ultrasound reconstructions by examining the eccentricity of the ellipsoids characterizing the images of the spherical phantom. First, we computed the medium axis ratio (r_{med}/r_{maj}) and the minor axis ratio (r_{min}/r_{maj}): in the ideal case all three radii lengths are equal and these ratios are equal to one. We also borrowed two metrics from the evaluation of diffusion anisotropy in diffusion tensor MRI imaging, calculating fractional anisotropy[18] and a spherical anisotropy metric $SA = 1 - (\lambda_3/\lambda_1)$.[19] Ideally, anisotropy is low for a perfect sphere and these metrics are equal to zero. The eccentricity results, listed in Table 3, showed a consistently excellent conservation of shape, with RMS medium and minor axis ratios of 0.98 and 0.97, respectively, for the images of the spherical phantom reconstructed using 3D ultrasound. The results from 4D ultrasound reconstruction are also very good, although slightly worse than those from 3D ultrasound reconstruction: the variability for both ratios increases compared to 3D ultrasound imaging, and although the RMS medium axis ratio is unchanged, the RMS minor axis ratio decreases to 0.95. The RMS fractional and spherical anisotropies were also small for both 3D and 4D ultrasound reconstruction, signifying a near-spherical object, and once again do increase slightly when comparing 4D ultrasound to 3D ultrasound.

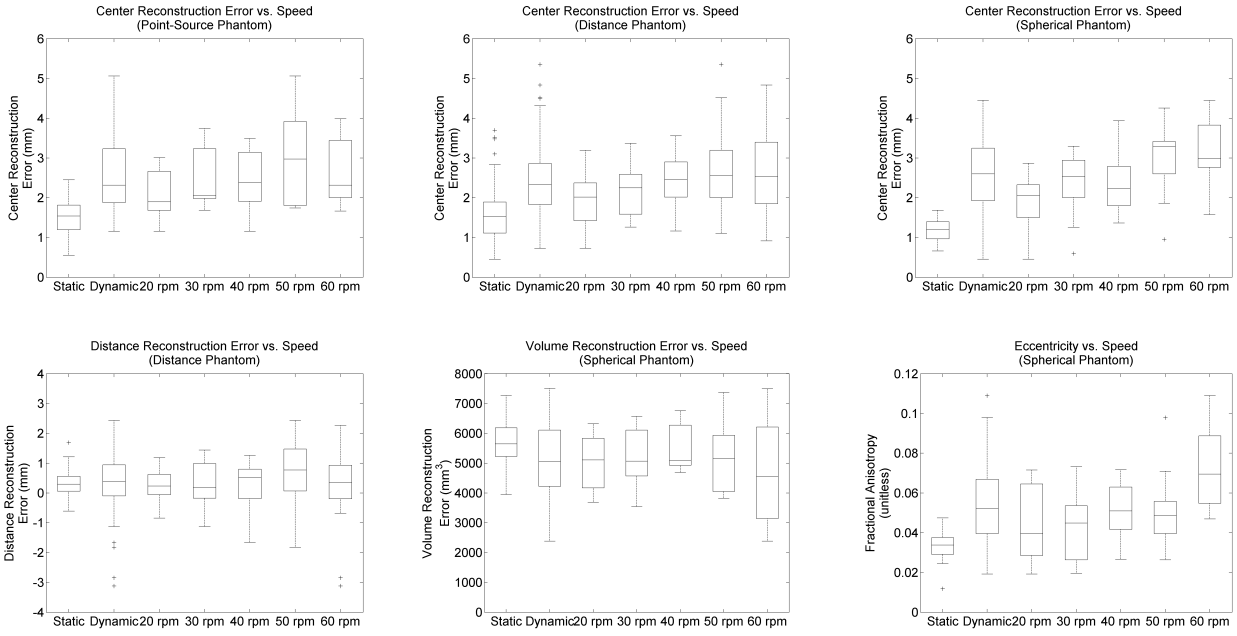

Figure 7: Center reconstruction error, distance reconstruction error, volume reconstruction error and fractional anisotropy for 4D ultrasound reconstruction versus phantom motor speed. Complete distributions for 3D ultrasound ('static') and 4D ultrasound ('dynamic') reconstruction errors are shown for comparison.

3.2 Relationship between 3D Ultrasound Reconstruction Accuracy and Depth

Plots of the 3D ultrasound reconstruction errors versus depth are shown in Figure 6. The center reconstruction errors for the point-source and distance phantoms show a strong depth dependency, which is not as apparent for the spherical phantom. For all three phantoms, plotting the center reconstruction error in the **y**-direction shows the most significant depth dependency of all three axes, and is particularly clear for the point-source and distance phantoms (plots not shown). We also found that volume reconstruction error has an inverse relationship with distance from the transducer, and that neither distance reconstruction error nor eccentricity are depth-dependent.

3.3 Relationship between 4D Ultrasound Reconstruction Accuracy and Speed

We are hesitant to draw conclusions regarding the dependence of 4D ultrasound reconstruction accuracy on the speed of the moving object, since $N = 10$ for each phantom for each motor speed tested, but do show the distributions of the 4D ultrasound reconstruction errors in Figure 7 as a function of speed. In general, the magnitude of the center reconstruction error has a tendency to increase with speed. The RMS values for distance reconstruction error and fractional anisotropy also increase with speed, although volume reconstruction error shows no consistent relationship.

4. DISCUSSION

In this study, we have extended a previous accuracy assessment protocol presented by our laboratory that evaluated the use of 2D ultrasound for surgical guidance[8] into the third and fourth dimensions. The RMS center reconstruction errors for 3D ultrasound reconstruction found in the present study, which ranged between 1.2 - 1.7 mm, are much better than the 2.4 mm RMS errors previously reported in the 2D ultrasound assessment. This is despite the fact that we used the same adult transesophageal probe and a highly-similar phantom design. The increase in accuracy when moving from 2D ultrasound to 3D ultrasound is most likely due to the averaging effect of 3D ultrasound reconstruction, where the errors associated with each individual 2D image are reduced as they are compounded together into a single volume. Additionally, since the previous study we have optimized the gain and compression settings on the ultrasound machine to maximize the strength of the edges defining the phantom boundaries, and have improved the gold standard phantom characterization by using a micro-CT image instead of digitizing the phantom surface using an optically-tracked pointer tool.

Despite the decrease in RMS errors between the 2D and 3D studies, some similarities in the results remain. The overestimation of both the distances between objects and the spherical phantom's radii lengths are consistent with the previous finding that area is overestimated under 2D ultrasound imaging. For the spherical object, this may be due to the technique employed to outline the images of the spherical phantom or because of the imaging properties of the table tennis ball, but are also consistent with a slow speed of sound within a 7% glycerol solution compared to the average speed of sound within tissue assumed by the ultrasound machine. The slow speed of sound hypothesis is also supported by the bias towards overestimating the distance between an object and the transducer in the depth direction. Further investigations into the optimal percentage of glycerol in water are ongoing within our laboratory.

Within our laboratory, we are interested in the accuracy with which preoperative images, such as those derived from MR or CT imaging, can be fused with intraoperative ultrasound imaging and registered to the patient anatomy. The results of our 4D ultrasound reconstruction accuracy assessment, which gave RMS center reconstruction errors ranging between 2.5 - 2.7 mm, are similar to those previously presented for 2D ultrasound guidance and are sufficient for use within our clinical context of minimally-invasive therapy applied to the beating heart. Although our reported errors for 3D ultrasound are larger than those found in similar 3D ultrasound reconstruction assessment studies, this may be attributed to the requirement for magnetic instead of optical tracking, and, more importantly, to the difficulty in manual segmentation of the image volumes. An automatic segmentation method would ideally be incorporated into the 3D ultrasound accuracy assessment protocol. However, the jitter found within image volumes derived from 4D ultrasound imaging makes automatic segmentation very difficult, and thus we elected to use manual segmentation to characterize all of the image volumes in this study for the sake of consistency.

In general, we found that moving from 3D to 4D ultrasound reconstruction leads to increased error magnitude and variability. This is primarily due to motion artifacts caused by the ECG-gated 4D ultrasound reconstruction

procedure, which increases the difficulty of the manual segmentation process for all three phantoms. These artifacts are depicted for our phantoms in Figure 4. Our observed 4D ultrasound reconstructions are similar to those found when imaging the beating heart, and so the quantitative results presented here are likely to approximate the errors that are present clinically when imaging the beating heart. The primary cause of the motion artifacts is the limited video capture rate achievable using the frame grabber, which causes inadequate sampling of the series of ultrasound images and is especially problematic when the object of interest moves at high speed. We insert the video frame whose timestamp is closest to the desired timestamp for a particular phase in the cardiac cycle, but the maximum time difference between these two is still approximately 15 ms. In this worst-case scenario, the phantom moves 0.4 mm when moving at 20 rpm and moves 1.26 mm when moving at 60 rpm. Access to the raw ultrasound data instead using of a frame grabber would decrease the significance of these artifacts.

Additional sources of error that are present within 4D ultrasound reconstruction but not in the 3D case include the use of prospective ECG-gating. Although our buffering scheme allows us to eliminate images acquired during large changes in patient heart rate, there is still error present within the 1.5% allowed deviation. In future, we will reduce this source of error by using retrospective ECG-gating instead of prospective ECG-gating. Interestingly, although one would expect that this error source would cause error to increase for later phases within the cardiac cycle, we have found no such relationship and in fact see several examples where the intermediate phases of the cardiac cycle are the least accurate. This effect may be because of the low sample size ($N = 10$) that we have for each phantom for each phase, and will be further studied.

Finally, we found that several ultrasound reconstruction errors were dependent on the axis of the image coordinate system. The increase in error of 4D ultrasound reconstruction compared to 3D ultrasound reconstruction was generally due to increased errors along the **y**- and **z**-directions, which are the two directions in which phantom movement was greatest and therefore the directions in which motion artifacts will be most significant. We also found that localization error increases with distance from the ultrasound transducer, which was not found in our laboratory's previous 2D ultrasound accuracy assessment study. This increase is likely because the distance between adjacent slices increases with depth when acquiring 3D and 4D ultrasound data around a rotational axis, decreasing the averaging effects of ultrasound reconstruction. In addition, partial volume effects increase with distance from the beam focus, causing blur and making it more difficult to manually identify small objects such as the spheres in the point-source and distance phantoms. Partial volume effects are also the most likely contributor to the observation that volume reconstruction error decreases with depth: since the outlines of the sphere were more blurry away from the transducer, our strategy of always selecting the outline closest to the fan origin decreased the size of the manually-identified sphere.

5. CONCLUSIONS AND FUTURE WORK

In this paper, we have described an accuracy assessment protocol for the evaluation of 4D ultrasound reconstruction using a dynamic phantom, and have additionally evaluated a newly-developed software package for real-time 3D and 4D ultrasound reconstruction. We conclude that the 3D and 4D reconstruction software meets the accuracy requirements for intraoperative imaging during minimally-invasive cardiac surgery, and will be further improved by replacing prospective ECG-gating with retrospective ECG-gating in the 4D ultrasound reconstruction process. Additional future work includes performing experiments to further evaluate the quality of temporal calibration by incorporating movement of the ultrasound transducer, and to begin utilizing the software within the operating room for enhanced surgical guidance within an augmented reality system.

ACKNOWLEDGMENTS

This work was supported by the Canadian Institutes of Health Research (CIHR), the Natural Science and Engineering Council of Canada (NSERC), the Ontario Research Development Challenge Fund (ORDCF), the Ontario Innovation Trust (OIT), the Canadian Foundation for Innovation (CFI) and the UWO Graduate Research Scholarships. The authors would also like to thank Dr. Dan Bainbridge, Dr. Gerard Guiraudon, Dr. Doug Jones, Dr. James White, Diane Liddle and Faisal Khan for their clinical assistance, Yogesh Thakur for suggestions regarding mechanical design, Dr. Joseph Umoh for micro-CT scanning and Diego Cantor for helpful discussions.

REFERENCES

[1] Linte, C., Moore, J., Wiles, A., Wedlake, C., and Peters, T., "Virtual reality-enhanced ultrasound guidance: A novel technique for intracardiac interventions," *Comput Aid Surg* **13**, 82–94 (2008).

[2] Lindseth, F., Lango, T., Bang, J., and Hernes, T. N., "Accuracy evaluation of a 3D ultrasound-based neuronavigation system," *Comput Aid Surg* **7**, 197–222 (2002).

[3] Rose, S., Hassanein, T., Easter, D., Gamagami, R., Bouvet, M., Pretorius, D., Nelson, T., Kinney, T., and James, G., "Value of three-dimensional US for optimizing guidance for ablating focal liver tumors," *J Vasc Interv Radiol* **12**, 507–515 (2001).

[4] Wei, Z., Gardi, L., Edirisinghe, C., Downey, D., and Fenster, A., "Three-dimensional ultrasound guidance and robot assistance for prostate brachytherapy," in [*Image-Guided Interventions: Technology and Applications*], Peters, T. and Cleary, K., eds., 429–460, Springer US (2008).

[5] Suematsu, Y., Martinez, J., Wolf, B., Marx, G., Stoll, J., DuPont, P., Howe, R., Triedman, J., and del Nido, P., "Thee-dimensional echo-guided beating heart surgery without cardiopulmonary bypass: Atrial septal defect closure in a swine model," *J Thorac Cardiovasc Surg* **130**, 1348–1357 (2005).

[6] Suematsu, Y., Kiaii, B., Bainbridge, D., del Nido, P., and Novick, R., "Robotic-assisted closure of atrial septal defect under real-time three-dimensional echo guide: in vitro study," *Eur J Cardio Thorac Surg* **32**, 573–576 (2007).

[7] Rousseau, F., Hellier, P., Letteboer, M., Niessen, W., and Barillot, C., "Quantitative evaluation of three calibration methods for 3-D freehand ultrasound," *IEEE Trans Med Imag* **25**, 1492–1501 (2006).

[8] Wiles, A., Moore, J., Linte, C., Wedlake, C., Ahmad, A., and Peters, T., "Object identification accuracy under ultrasound enhanced virtual reality for minimally invasive cardiac surgery," in [*Medical Imaging: Visualization, Image-Guided Procedures, and Modelling*], Miga, M. and Cleary, K., eds., *SPIE 2008* **6918**, 39180E (2008).

[9] Gobbi, D. and Peters, T., "Interactive intra-operative 3D ultrasound reconstruction and visualization," in [*Medical Image Computing and Computer-Assisted Interventions*], Dohi, T. and Kikinis, R., eds., **LNCS 2489**, 156–163 (2002).

[10] Boisvert, J., Gobbi, D., Vikal, S., Rohling, R., Fichtinger, G., and Abolmaesumi, P., "An open-source solution for interactive acquisition, processing and transfer of interventional ultrasound images," in [*Workshop on Systems and Architectures for Computer Assisted Interventions*], **MICCAI 2008** (2008).

[11] Barratt, D., Davies, A., Hughes, A., Thom, S., and Humphries, K., "Accuracy of an electromagnetic three-dimensional ultrasound system for carotid artery imaging," *Ultrasound Med Biol* **27**, 1421–1425 (2001).

[12] Pace, D., Kikinis, R., and Hata, N., "An accessible, hands-on tutorial system for image-guided therapy and medical robotics using a robot and open source software," in [*Workshop on Open Source and Open Data*], **MICCAI 2007** (2007).

[13] Gobbi, D., Comeau, R., and Peters, T., "Ultrasound probe tracking for real-time ultrasound/MRI overlay and visualization of brain shift," in [*Medical Image Computing and Computer-Assisted Interventions*], Taylor, C. and Colchester, A., eds., **LNCS 1679**, 920–927 (1999).

[14] Gobbi, D., *Brain deformation correction using interactive 3D ultrasound imaging*, PhD thesis, Department of Medical Biophysics, The University of Western Ontario, London, Canada (2003).

[15] Forbes, A., "Least-squares best-fit geometric elements," Tech. Rep. NPL Report DITC 140/89, National Physical Laboratory (April 1989).

[16] Li, Q. and Griffiths, J., "Least squares ellipsoid specific fitting," in [*Geometric Modeling and Processing*], 335–340, IEEE Computer Society (2004).

[17] Schneider, P. and Eberly, D., [*Geometric tools for computer graphics*], Morgan Kaufmann (2002).

[18] Le Bihan, D., Mangin, J.-F., Poupon, C., Clark, C., Pappata, S., Molko, N., and Chabriat, H., "Diffusion tensor imaging: Concepts and applications," *J Magn Reson Imag* **13**, 534–546 (2001).

[19] Westin, C., Maier, S., Khidhir, B., Everett, P., Jolesz, F., and Kikinis, R., "Image processing for diffusion tensor magnetic resonance imaging," in [*Medical Image Computing and Computer-Assisted Interventions*], Taylor, C. and Colchester, A., eds., **LNCS 1679**, 441–452 (1999).